



# Experimental and Numerical Study on Failure Modes and Shear Strength Parameters of Rock-Like Specimens Containing Two Infilled Flaws

Wuchao Wang<sup>1</sup> · Shaorui Sun<sup>1</sup> · Huilin Le<sup>1</sup> · Yang Shu<sup>2</sup> · Feng Zhu<sup>1</sup> · Haotian Fan<sup>1</sup> · Yong Liu<sup>1</sup>

Received: 15 March 2019 / Revised: 10 June 2019 / Accepted: 19 June 2019 / Published online: 8 July 2019  
© Iran University of Science and Technology 2019

## Abstract

To investigate the influence of infilled flaws on mechanical properties and failure modes of rock masses, seven types of pre-existing infilled two-flaw specimens, which have different flaw inclination angle ( $\alpha$ ), rock bridge length ( $L_2$ ) and rock bridge inclination angle ( $\beta$ ), were made from concrete. The crack coalescence process, failure modes and mechanical parameters of the specimens under triaxial or biaxial compression were studied by lab test and numerical tests, respectively. According to test results, two failure modes of specimen (shear failure, tensile–shear failure) and three rock bridge coalescence modes (tensile crack coalescence, shear crack coalescence, no coalescence) were identified. As the rock bridge length and inclination angle increase, the peak strengths of specimens also increase gradually, while the peak strengths of specimens decrease with flaw inclination angle being increase. The shear strength parameters (cohesion  $c$  and internal friction angle  $\varphi$ ) of samples show nonlinear changes with various factors (flaw angle, rock bridge length, rock bridge angle). The particle flow code (PFC) was used to simulate the propagation process of microcracks and porosities, stress–strain curves for loading process were also obtained, numerical results are in good agreement with experimental results. The number of cracks and porosities increase rapidly in the post-peak stage, and a significant shear fracture zone was caused by cracks. This study provides a better understanding of peak strength and cracking behaviour of rock mass containing infilled flaws.

**Keywords** Two infilled flaws · Triaxial compression test · Numerical simulation · Failure mode · Shear strength parameter

## 1 Introduction

Many engineering cases show that the deformation and instability of rock masses are largely affected by flaws in the rock mass [1–3]. Fractured rock masses are widely distributed and play an important role in engineering

projects. Therefore, it is of great theoretical and practical significance to study the mechanical properties and failure modes of fractured rock masses.

In laboratory tests, some scholars have performed uniaxial, biaxial and triaxial tests to study the mechanical behaviours of rock-like specimens with pre-existing flaws

✉ Shaorui Sun  
ssrfish@hhu.edu.cn

Wuchao Wang  
wangwuchao@hhu.edu.cn

Huilin Le  
lehuilin@hhu.edu.cn

Yang Shu  
282818073@qq.com

Feng Zhu  
160211090004@hhu.edu.cn

Haotian Fan  
fanhaotian@hhu.edu.cn

Yong Liu  
dayoga@hhu.edu.cn

<sup>1</sup> School of Earth Sciences and Engineering, Hohai University, Nanjing, Jiangsu, China

<sup>2</sup> China Railway Eryuan Engineering Group Co. Ltd., Chengdu, Jiangsu, China

of different geometries [4–8]. Sun et al. [9] carried out uniaxial compressive tests on rock-like specimens containing pre-existing flaws with different inclination angles. They found that specimens containing flaws with inclination angles of  $45^{\circ}$ – $60^{\circ}$  fail easily under compression. Cao et al. [10] investigated the peak strength and failure mode of rock-like specimens with multiple flaws. The test results showed that the coalescence modes of the flaws can be classified into three categories: S-mode, T-mode, and M-mode. Moreover, the failure modes can be classified into four categories: mixed failure, shear failure, stepped path failure, and intact failure. Zhao et al. [11] obtained several modes of crack propagation under uniaxial loading by installing a strain gauge at flaw tips, which are similar to the conclusions obtained by Cao et al. [10]. Cao et al. [12] carried out uniaxial compression tests on specimens with three pre-existing flaws and found that as the rock bridge angle increases, the failure mode of the specimens changed from wing crack propagation failure to crack coalescence failure. Based on test results, the influence of both the number and inclination angles of pre-existing cracks on crack growth was analysed by Wang et al. [13]. The fractal dimension was adopted to quantitatively describe crack growth during the failure process. Huang et al. [14] used the acoustic emission (AE) monitoring technique to record the failure process of pre-flawed specimens. When crack coalescence occurred or a crack was initiated, a large AE event could be observed simultaneously, and the corresponding axial stress dropped in the axial stress–time curve. This technique provides a new method for studying crack propagation in rock-like materials. Feng et al. [15] observed the mechanical properties and coalescence behaviours of intact and fissured specimens under four static pre-stress and three strain rates. All specimens showed tensile splitting failure and could be divided into five penetration modes. In triaxial tests, the confining pressure had significant effects on the crack coalescence process and the failure patterns of rock-like specimens [16]. Xiao et al. [17] found that the confining pressure had a significant impact on the peak strength, residual strength and ductility characteristics of the specimen.

However, most of the above studies focus on specimens with unfilled flaws. In fact, fractures in rock masses are often infilled, which has an important effect on the mechanical behaviour of rock masses. Therefore, some scholars [18–20] have carried out uniaxial and triaxial compression tests on specimens with pre-existing flaws to study the strength, failure modes and crack propagation characteristics. Filling materials are usually gypsum, cement paste, and sandy clay [21–24]. Infilled flaws can weaken the shear strength of specimens, and the degree of weakening is affected by many factors, such as the thickness and strength of filling materials [25–27]. With

continuous improvement in computing ability, more numerical methods have been applied to solve engineering problems. Many numerical methods have been used to study the fracture mechanisms of rock masses. Researchers have used PFC<sup>2D</sup>, RFPA<sup>2D</sup>, FLAC<sup>3D</sup> and other software to analyse the propagation processes of micro-cracks [5, 28, 29]. It is found that cracks in any two flaws follow the lowest intensity path under uniaxial compression. Many scholars have conducted numerical experiments on fractured rock masses under different conditions, which prove the feasibility of numerical experiments [10, 30, 31].

At present, research on the mechanical behaviours of artificial specimens with unfilled flaws is more comprehensive. However, there has been relatively little research conducted on the mechanical behaviour of specimens with infilled flaws. In engineering practice, epoxy resin is widely used in engineering to reinforce fractured rock masses, but research on the mechanical properties of specimens containing flaws infilled with epoxy resin is rare. And epoxy resin material has high strength, easy to control solidification time, stable bonding performance and different bonding strength can be achieved by different mixing proportion. Therefore, epoxy resin was selected as filling material in this research. In addition, most current experimental studies are focused on uniaxial or biaxial compression tests on pre-existing samples [32–35]. In fact, the occurrence conditions of rock masses in nature are complex, and triaxial tests can more accurately reflect the mechanical characteristics of rock masses under complex geological conditions. As a result, triaxial tests were selected for laboratory testing. However, the failure process of specimens is difficult to observe in triaxial tests. Therefore, the particle flow code (PFC) was used to simulate the triaxial tests and monitor the cracking processes and porosity.

## 2 Specimen Preparation and Test Methods

### 2.1 Specimen Preparation

Because of the complex distribution of fractures in natural rock masses, it is difficult to make real rock specimens with specific flaws in the laboratory and carry out repeatable tests. In this paper, C42.5 Portland cement, quartz sand and water were used to make rock-like specimens at a weight ratio of 1:2:0.45. The mixture was poured into the mould, and then a steel sheet was inserted into the mixture. Later, the mould was placed in a curing box with a constant temperature of  $26^{\circ}\text{C}$  and a humidity of 95%. After 28 days, the cured samples were drilled and cut to make cylindrical specimens with diameters of 50 mm and heights of 100 mm. Epoxy resin was chosen as the grouting

material to fill the pre-existing flaw. The epoxy resin was a mixture of epoxy acrylate latex and curing agent in weight proportions of 2:1. The grouting material and mixing ratio were the same as those in Le et al. [36]. Le et al. [36] showed that the epoxy resin uniaxial compressive strength, internal friction angle and cohesive force are 42.0 MPa,  $41.6^\circ$  and 10 MPa, respectively. The grouting material took 3 days to solidify. The chosen flaw angles were  $30^\circ$ ,  $45^\circ$  and  $60^\circ$ . The reason is that many specimen failure surfaces appear at angles between  $30^\circ$  and  $60^\circ$  to the horizontal plane [37]. The geometry of the flaws tested is shown in Fig. 1. The geometries of flaws are determined by four parameters: the flaw length  $L_1$ , flaw angle  $\alpha$ , rock bridge length  $L_2$  and rock bridge angle  $\beta$ .

## 2.2 Test Methods

Seven kinds of specimens (A–G) were designed in this experiment (see Table 1). Repeated tests were carried out on three identical samples in each group to avoid incidental results. The triaxial system was produced by ELE (England), and its maximum confining pressure and accuracy were 70 MPa and 1%, respectively. The testing procedures for triaxial compression test complied with the ASTM [38]. The test system consisted of three parts: a confining pressure control system, an axial pressure control system and a digital display device (see Fig. 2). Triaxial compression tests were carried out under confining pressures of 1.0, 2.0, 3.0 and 4.0 MPa until the samples failed. During the tests, the confining pressure was loaded to the predetermined value at a rate of 15 kPa/s. The axial pressure was loaded at a rate of 2 kN/min until the sample failed. The shear strength of the intact specimens was measured by the triaxial compression test. The cohesion  $c$  was 11.09 MPa, and the internal friction angle  $\varphi$  was  $41.60^\circ$ .

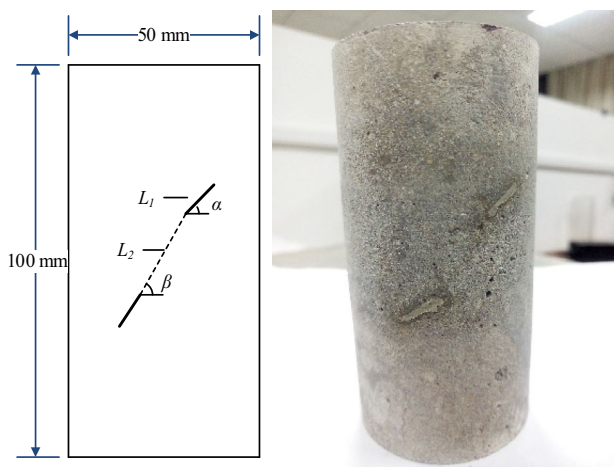


Fig. 1 Geometry of flaws in rock-like specimens

**Table 1** Geometric parameters of rock-like material specimens containing two flaws

Specimen group	$L_1/\text{cm}$	$\alpha/^\circ$	$L_2/\text{cm}$	$\beta/^\circ$
A	1	30	2	90
B	1	30	3	90
C	1	30	4	90
D	1	30	2	60
E	1	30	2	120
F	1	45	2	60
G	1	60	2	60

## 3 Laboratory Test Results and Analysis

Based on previous studies [11, 39–43], the cracks observed in the specimens are classified into four types: tensile cracks (in this research, tensile cracks were divided into two types:  $T_a$  and  $T_b$ .  $T_a$  refers to tensile cracks observed at the external flaw tip area, and  $T_b$  refers to tensile cracks observed at the inner flaw tip area), anti-tensile cracks (AT), coplanar shear cracks (CS) and inclined shear cracks (IS). The tensile and anti-tensile cracks initiate from the tips of the pre-existing flaws and usually develop along the direction of the maximum principal stress. There are two kinds of shear cracks: coplanar shear cracks, which propagate along the plane of the pre-existing flaw, and inclined shear cracks, which initiate from the tips of the pre-existing flaws and propagate along the vertical direction of the coplanar crack. The locations of the tips of the two flaws are shown in Fig. 3b. The term “flaw” represents the pre-existing flaw, and the term “crack” represents a new fracture that occurs during the compression test.

### 3.1 Crack Evolution Analysis for Specimens with Different Rock Bridge Lengths

When  $L_2 = 3$  cm and 4 cm, rock bridges of specimens were mainly connected by tensile cracks  $T_b$  that occurred at the inner flaw tips (Fig. 4b, c). Meanwhile, tensile cracks  $T_a$  initiated at external flaw tips and then propagated towards the top and bottom of the specimens (Fig. 4, models C1 and C4). Some tensile cracks ( $T_a$ ) first propagated along the maximum principal stress and then developed along an inclined trajectory towards the left and right edge of the sample (Fig. 4, models B1 and B3). These cracks ( $T_a$ ) formed the main failure path and caused the tensile–shear failure of the specimens. The rock bridge was connected by these cracks. This failure mode is called type I. Coplanar shear cracks (CS) and inclined shear cracks (IS) could be observed at flaw tips under low confining pressure, and shear cracks could not be found at high confining



Fig. 2 Triaxial system

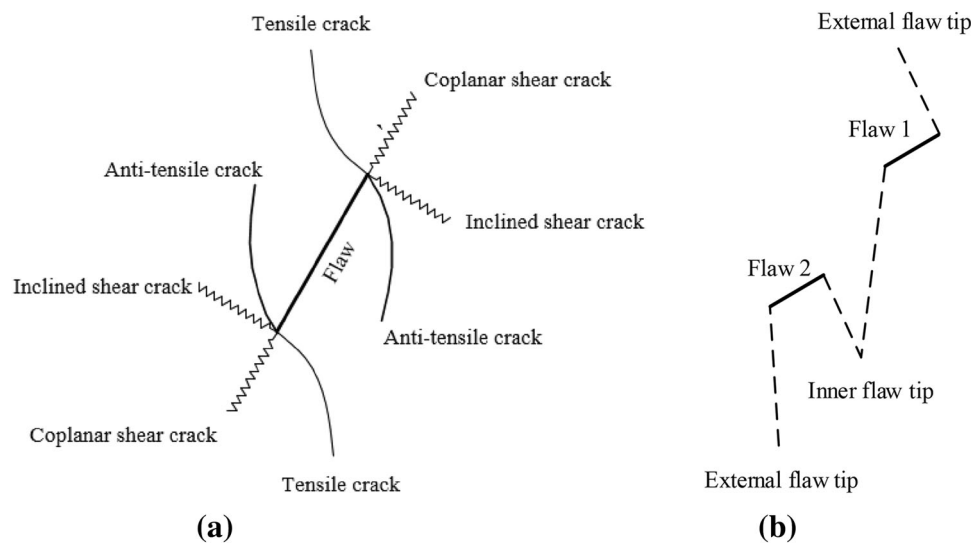


Fig. 3 Crack types and flaw tip definitions

pressure. When  $L_2 = 2$  cm, tensile cracks, anti-tensile cracks (AT) and coplanar shear cracks were observed in the specimens (Fig. 4, models A1 and A2). The main failure path was caused by tensile cracks, and the specimen failure mode was type I. When  $\sigma_3 = 3.0$  MPa and 4.0 MPa, inclined shear cracks initiated from the inner tip of flaw 1 and propagated along an inclined trajectory towards the top and bottom boundary of the sample, which formed a failure plane and led to the shear failure of the specimens (Fig. 4, models A3 and A4). The specimens showed shear failure, and the rock bridge was not connected. This failure mode is called type II.

Under the condition of different rock bridge lengths, the macroscopic failure modes of specimens are mainly tensile–shear failure (type I) and shear failure (type II). With increasing bridge length, it is easier for the rock bridge to be cut through by tensile cracks initiating from the inner

tips of pre-existing flaws. The tensile stress is more concentrated in the middle part of the specimen and tensile–shear failure (type I) is more common.

### 3.2 Crack Evolution Analysis for Specimens with Different Rock Bridge Angles

In group D (Fig. 5a), coplanar shear cracks CS that initiated at external flaw tips extended a certain distance outward, while the cracks  $T_a$  deflected and extended along the direction of the major principal stress and then cut through the top and bottom of the specimen. Coplanar shear cracks CS were also found at internal flaw tips. These cracks extended a slight distance inward first and then propagated through the whole rock bridge area by tensile cracks  $T_b$ . The failure mode of specimens was tensile–shear failure (type I). When  $\beta = 90^\circ$  (Fig. 4a, group A), with increasing

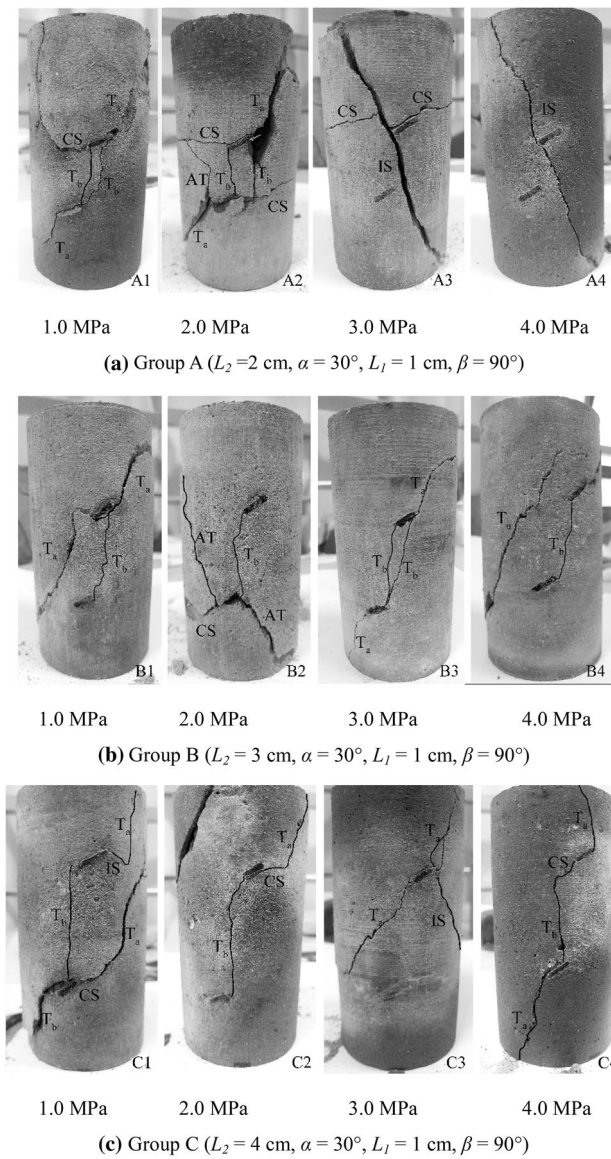


Fig. 4 Failure modes of specimens with different rock bridge lengths

confining pressure, inclined shear cracks IS formed the main failure path, and the failure mode changed from tensile–shear failure (type I) to shear failure (type II). When  $\beta = 120^\circ$  (Fig. 5b, group E), two flaws were parallel, and a number of cracks occurred in the specimens and led to complex failure. Many fragments were produced in the process of compression. When  $\sigma_3 = 1.0$  and 4.0 MPa (Fig. 5b, models E1 and E4), tensile cracks  $T_a$  and anti-tensile cracks AT propagated along the direction of principal stress and developed to the top and bottom edges. The failure mode was tensile–shear failure, but the rock bridge was not cut through. This failure mode is called type III. When  $\sigma_3 = 2.0$  MPa (Fig. 5b, model E2), cracks CS and IS occurred at the external tip of flaw 1, and these cracks formed X-shaped failure planes in the specimen. When

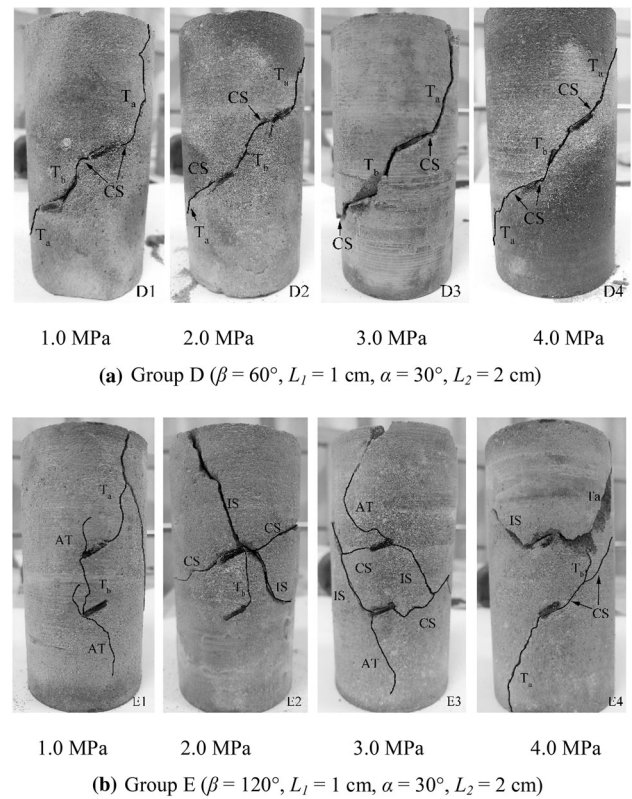


Fig. 5 Failure modes of specimens with different rock bridge angles

$\sigma_3 = 3.0$  MPa (Fig. 5b, model E3), coplanar shear cracks CS and inclined shear cracks IS coalesced, which formed an elliptical core in the middle of the specimen. Anti-tensile cracks AT initiated at the flaw tips and developed to the top and bottom of the specimen, and the failure mode was tensile–shear failure (type III).

For the specimens with different bridge angles, the failure modes are mainly tensile–shear failure in which rock bridges are cut through (type I), shear failure (type II) and tensile–shear failure in which rock bridges are not cut through (type III). As the bridge angle  $\beta$  increases from  $60^\circ$  to  $120^\circ$ , anti-tensile cracks and inclined shear cracks begin to develop and gradually become the main crack categories in the specimen. The crack trajectories in the specimen become more complex, and the failure mode of specimens changes from type I to type III.

### 3.3 Crack Evolution Analysis for Specimens with Different Flaw Angles

Typical failure plots of specimens with different flaw angles are shown in Fig. 6. The coplanar shear cracks initiated at the flaw tips of the specimen penetrated the rock bridge and both edges of specimens under different confining pressures (Fig. 6a). The failure mode of specimens was shear failure (type II). In group G, the flaw angle of the

specimen was the same as that of the rock bridge (Fig. 6b). The flaws and rock bridge were collinear. Crack propagation in the specimens under different confining pressures was similar. Tensile cracks  $T_a$  that initiated at flaw tips penetrated the top and bottom of the specimens. The rock bridge was cut through a coplanar shear crack. When  $\sigma_3 = 1.0$  and 3.0 MPa (Fig. 6b, models G1 and G3), anti-tensile cracks appeared in the specimens, and most specimens showed obvious tensile–shear failure (type I). When  $\sigma_3 = 2.0$  MPa (Fig. 6b, model G2), a group of inclined shear cracks developed at the inner tip of flaw 1, and these cracks formed X-shaped failure plane in the specimen. The specimen failure mode showed shear failure (type II).

With increasing flaw angle, the geometric characteristics between rock bridge and flaws change from non-collinear to collinear, and the destruction form of the rock bridge changes from tensile crack ( $T_b$ ) perforation failure to coplanar shear crack (CS) perforation failure. More tensile cracks ( $T_a$  and  $T_b$ ) appear in specimens with flaw angles of  $30^\circ$  and  $60^\circ$  (group D and group G). The tensile stress in the middle of the specimens is large. However, the coplanar shear cracks that develop in the specimens with  $\alpha = 45^\circ$  (group F) indicate that the tensile stress in the middle of the specimens is small. The failure mode of the specimen changes from tensile–shear failure to shear failure and then to tensile–shear failure (group D  $\rightarrow$  group F  $\rightarrow$  group G).

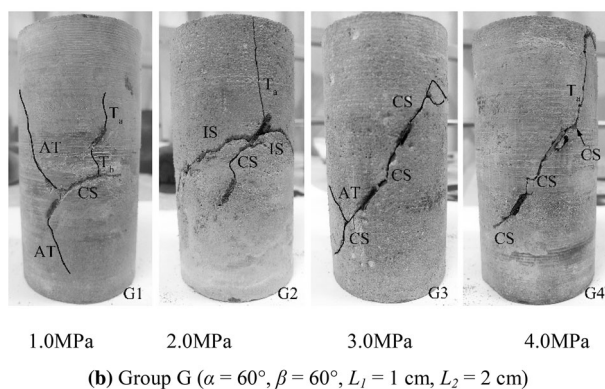
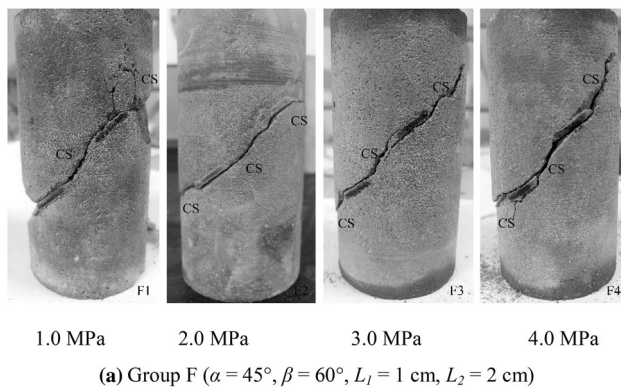


**Fig. 6** Failure modes of specimens with different flaw angles

### 3.4 Analysis of the Strength and Mechanical Parameters of the Specimens

Table 2 and Fig. 7a show that as the length of the rock bridge increases, the peak strength of specimens increases gradually. When the bridge length is large, the interaction between two flaws is weak; it is difficult for cracks to initiate, develop and coalesce; therefore, the specimens with a longer bridge length have a larger compressive strength. Figure 7b indicates that with increasing rock bridge inclination angle, the peak strength of the specimens increases. With increasing rock bridge inclination angle, the angle between the rock bridge and fracture surface of the intact specimen increases gradually, and the initiation, propagation, and penetration of rock bridge cracks are restrained, which makes it difficult for rock bridge to be destroyed; thus, the failure strength of the specimen increases. On the other hand, when the rock bridge angle is  $120^\circ$ , the two flaws are parallel, forming a certain degree of shielding effect on crack propagation, thereby enhancing the failure strength of the specimens. From Fig. 7c, when the flaw angle increases from  $30^\circ$  to  $60^\circ$ , the strength of the specimen decreases gradually and reaches the lowest when the flaw angle is  $60^\circ$ . This result is mainly due to the improvement of the collinearity between the two flaws, which makes the connection between the flaws and the rock bridge approximately equal to the fracture surface of the complete specimen, and the cracks more easily penetrate the specimen.

Figure 8a shows that the cohesion of the specimens decreases as the bridge length increases from 2 to 3 cm and then increases as the bridge length increases from 3 to 4 cm. The internal friction angle of the specimens increases as the bridge length increases from 2 to 3 cm and decreases as the bridge length increases from 3 to 4 cm. From Fig. 8b, when the rock bridge angle increases gradually, the internal friction angle decreases continuously, while the cohesion increases continuously, reaching the minimum internal friction angle and the maximum

**Table 2** Peak strength of specimens with two infilled flaws and intact

Specimen group	Confining pressure (MPa)			
	1.0	2.0	3.0	4.0
A ( $L_2 = 2$ cm, $\alpha = 30^\circ$ , $\beta = 90^\circ$ )	42.02	49.47	55.38	59.34
B ( $L_2 = 3$ cm, $\alpha = 30^\circ$ , $\beta = 90^\circ$ )	43.56	51.42	58.73	63.97
C ( $L_2 = 4$ cm, $\alpha = 30^\circ$ , $\beta = 90^\circ$ )	45.37	57.02	60.73	64.07
D ( $L_2 = 2$ cm, $\alpha = 30^\circ$ , $\beta = 60^\circ$ )	35.25	47.28	52.58	55.46
E ( $L_2 = 2$ cm, $\alpha = 30^\circ$ , $\beta = 120^\circ$ )	49.05	52.39	57.48	61.25
F ( $L_2 = 2$ cm, $\alpha = 45^\circ$ , $\beta = 60^\circ$ )	34.75	44.49	48.68	51.39
G ( $L_2 = 2$ cm, $\alpha = 60^\circ$ , $\beta = 60^\circ$ )	31.62	34.02	44.29	47.29
Intact specimen	53.25	60.52	62.92	70.51

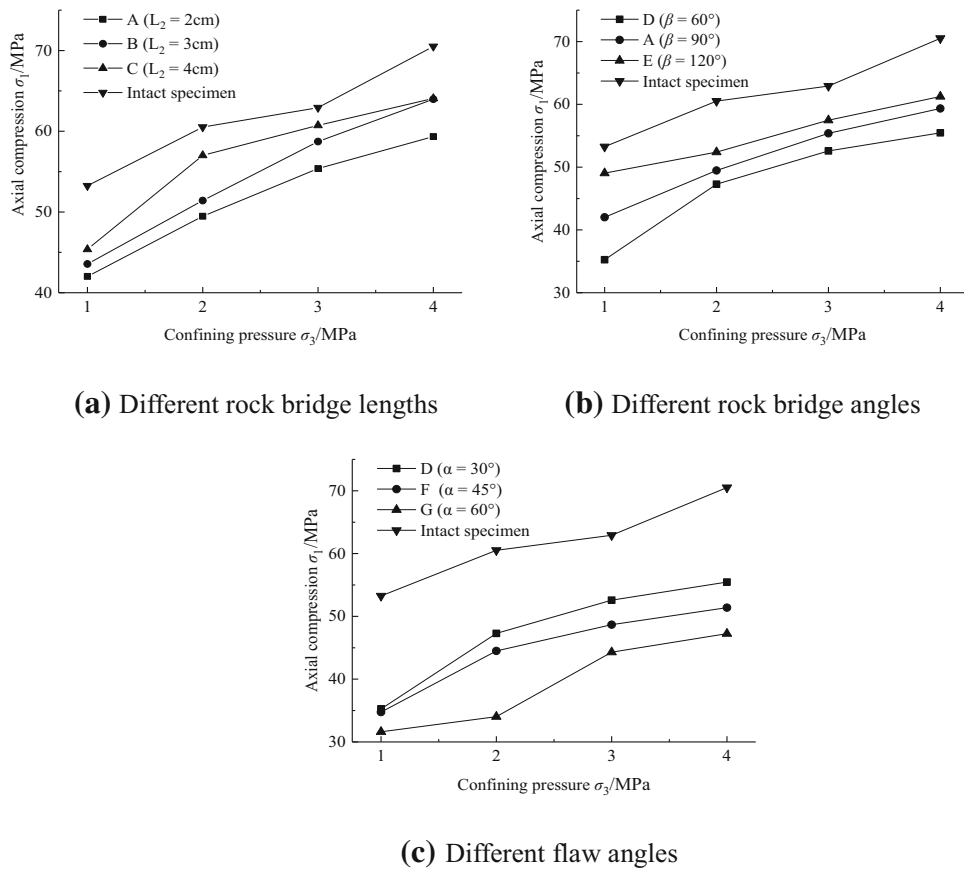


Fig. 7 Influence of various factors on specimen failure strength

cohesion at  $120^\circ$ . When the fracture angle increases, the cohesion of specimens increases as the fracture angle increases from  $60^\circ$  to  $90^\circ$  and then decreases as the fracture angle increases from  $90^\circ$  to  $120^\circ$ . The internal friction angle of the specimens decreases as the fracture angle increases from  $60^\circ$  to  $90^\circ$  and decreases as the fracture angle increases from  $90^\circ$  to  $120^\circ$ . As can be seen from Table 3, the angle clearly has a greater influence on the mechanical parameters of the specimen than the length.

### 3.5 Comparison with a Similar Study

Similar triaxial compression tests on two pre-existing unfilled flaw specimens were conducted by Sun [44]. This study involved a series of specimens with different flaw geometries, and crack coalescence processes were observed. When the rock bridge angle was  $90^\circ$  and the flaw angle was  $30^\circ$ , the cracks tended to propagate along the principal stress direction and formed tensile cracks in

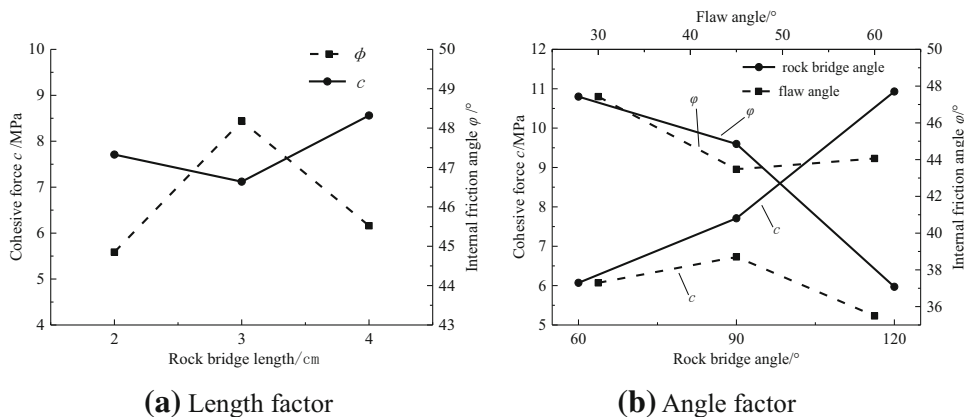


Fig. 8 Influence of various factors on the mechanical parameters of specimens

unfilled flaw specimens (see Fig. 9b). However, coplanar shear cracks were observed from the flaws infilled with epoxy resin for the same geometry (see Fig. 4, A1 and A2). The reason for this phenomenon is that unfilled flaws form narrow cavities in the specimen. When the confining pressure and axial pressure act on the specimen, tensile stress concentration occurs at the flaw tips; when epoxy resin fills the cavity and forms a channel for stress transfer, stress concentration at the flaw tip is alleviated. Cracks develop more easily along the interface between the model material and grouting material in specimens with infilled flaws than in specimens with unfilled flaws. The peak strength and strength parameters of specimens with two infilled flaws or unfilled flaws are also shown in Table 4. The mechanical properties of the specimens are significantly improved after the epoxy resin is infilled.

Epoxy resin was also used to make specimens with a single flaw. Uniaxial compression tests on specimens with a single pre-existing infilled flaw were conducted by Le et al. [45]. In this paper, the specimen failure paths were observed and compared between flaws grouted with cement and flaws grouted with epoxy resin. The cracks developed to the lateral edges when the pre-existing flaw was infilled with cement, while the crack propagated along the direction of axial stress when the flaw was infilled with epoxy resin. This conclusion is contrary to the phenomenon observed in the triaxial compression tests. The reason is that the confining pressure in triaxial compression tests limits radial deformation and affects the stress distribution near the flaw. Le et al. [36] found that the uniaxial compressive strength of the specimens grouted with epoxy resin fluctuated within a range from 39.1 to 42.6 MPa. This

**Table 3** Mechanical parameters of infilled double-flaw specimens

Specimen group	Mechanical parameters	
	Cohesive force (MPa)	Internal friction angle (°)
A ( $L_2 = 2$ cm, $\alpha = 30^\circ$ , $\beta = 90^\circ$ )	7.71	44.85
B ( $L_2 = 3$ cm, $\alpha = 30^\circ$ , $\beta = 90^\circ$ )	7.12	48.18
C ( $L_2 = 4$ cm, $\alpha = 30^\circ$ , $\beta = 90^\circ$ )	8.56	45.52
D ( $L_2 = 2$ cm, $\alpha = 30^\circ$ , $\beta = 60^\circ$ )	6.07	47.43
E ( $L_2 = 2$ cm, $\alpha = 30^\circ$ , $\beta = 120^\circ$ )	10.93	37.08
F ( $L_2 = 2$ cm, $\alpha = 45^\circ$ , $\beta = 60^\circ$ )	6.73	43.47
G ( $L_2 = 2$ cm, $\alpha = 60^\circ$ , $\beta = 60^\circ$ )	5.23	44.06
Intact specimen	11.09	41.60

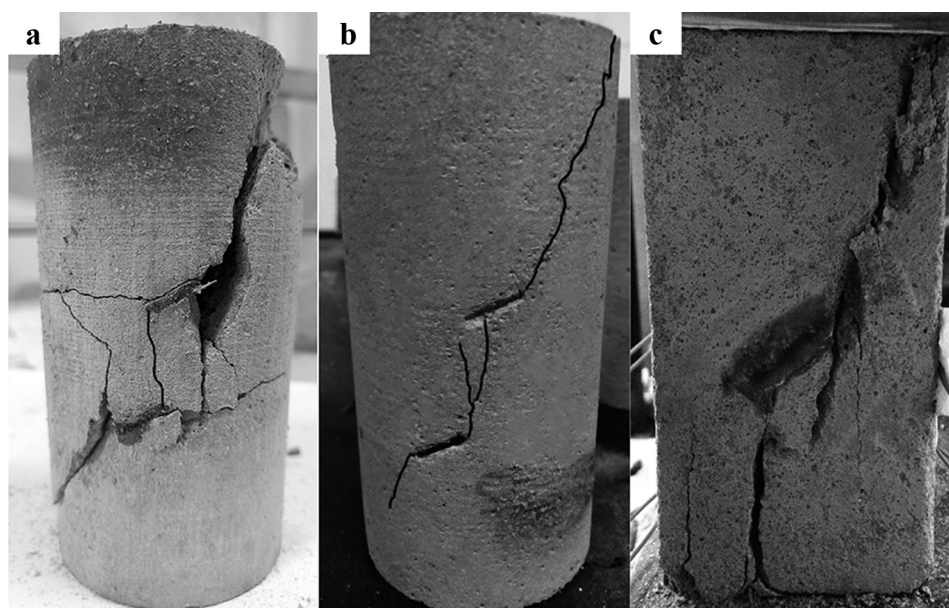


**Fig. 9** Comparison of failure patterns with different specimens: **a** specimen A2; **b** unfilled flaw specimen with a flaw angle of  $30^\circ$  and a rock bridge angle of  $90^\circ$  [44]; **c** specimens with a single infilled flaw grouted with epoxy resin with an inclination angle of  $45^\circ$  [45]



**Table 4** Peak strength and strength parameters for different specimen types in triaxial compression tests

Specimen type	Confining pressure (MPa)				Mechanical parameters	
	1.0	2.0	3.0	4.0	Cohesive force (MPa)	Internal friction angle (°)
Specimens with two unfilled flaws [44]	30.48	31.70	37.33	41.22	6.5	35.6
Specimens with two infilled flaws	42.02	49.47	55.38	59.34	7.71	44.85

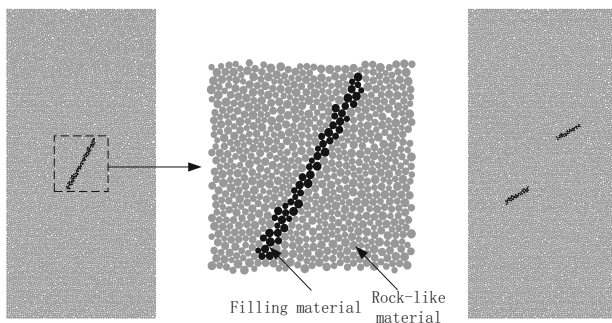
result indicates that epoxy resin has a good reinforcement effect on a fractured rock mass.

Zhuang et al. [46] fills the flaws with gypsum and then carries out uniaxial compression tests on the specimens. The study found that initiation angle of wing cracks decreases as the flaw angles increase. However, the values of initiation angle with unfilled flaw are larger than those with filled flaw for the same flaw angle. The anti-wing crack initiation location is not at the tips of the flaw but at a small distance to the tips. Secondary cracks as shear cracks appeared after the wing cracks and anti-wing cracks, and always initiated at a distance from the tips. The test results in this paper also show the same rule. It shows that both gypsum and epoxy resin can be effectively reduced the stress concentration at the flaw tips.

## 4 Numerical Tests and Analysis of Results

### 4.1 Numerical Test Model and Parameters

The evolution laws for cracks, porosity changes and failure modes of double-flaw infilled specimens during loading are analysed by numerical testing using the two-dimensional particle flow code (PFC2D). A 50 mm × 100 mm model is established in the numerical tests. The maximum and minimum particle radii are 0.45 mm and 0.3 mm, respectively. Because the parallel bond model can better reflect the physical and mechanical properties of brittle rock materials [47], the parallel bond model between particles is adopted (see Fig. 10). By adjusting the microscopic parameters of the sample material and the filling material

**Fig. 10** PFC<sup>2D</sup> numerical test model for filling flaws

(epoxy resin) by the trial and error method [48], the simulated results are approximately matched with the laboratory test results (strength value, failure mode) to obtain the complete microscopic parameters of the sample. The microscopic parameters of the model are shown in Tables 5 and 6. To verify the rationality of the selection of the micro-parameters of the numerical model, the failure strength values of each group of specimens under a confining pressure of 1 MPa are compared with those of the numerical tests. From Table 7, it can be seen that the deviations between the strengths from the numerical tests and the laboratory tests are small, so the model can meet the requirements of the numerical test.

### 4.2 Numerical Test Results

Figures 11 and 12 show the stress–strain curves of specimens with different rock bridge lengths under a confining pressure of 1 MPa and the distribution of cracks in the specimens after loading. The numerical test model flaw angle is 30°, and the rock bridge angle is 90°. The larger the rock bridge length is, the higher the peak strength of the specimen, the larger the number of cracks in the specimen, the less obvious the fracture zone, and the more complicated the crack trace. Under different rock bridge lengths, the number of cracks in the specimen increases slowly at first and then rapidly. The growth rate is the fastest after peak strain, and most of the cracks are produced after peak strain. When the length of the rock bridge is 2 cm, the rock bridge is connected by tensile cracks, and the tensile cracks initiate at external flaw tips and then propagate towards the top and bottom of the specimens. The two tensile cracks in the rock bridge area form a jujube-shaped crack ring. The failure mode of the specimen is tensile–shear failure. When the length of the rock bridge is 3 cm, the rock bridge is cut through by tensile cracks, and a group of tensile cracks and anti-tensile cracks initiate from the external fissures tip and cause the tensile–shear failure of the specimens. When the length of the rock bridge is 4 cm, the rock bridge is not connected, and an inclined shear crack is initiated from the external crack tip, which results in the shear failure of the specimen. From the numerical test results, the strengths and failure modes of the specimens are in good agreement with those from the laboratory tests.

**Table 5** Micro-mechanical parameters for rock-like material in PFC<sup>2D</sup>

Micro-parameters	Values	Remarks
Density of the ball (kg m <sup>-3</sup> )	2200	Parameter of ball
Friction coefficient	0.3	Parameter of ball
Minimum radius of the ball (mm)	0.3	Parameter of ball
Ratio of maximum to minimum of radius	1.5	Parameter of ball
Young's modulus of the ball (GPa)	14.6	Parameter of ball
Ratio of normal to shear stiffness of the ball	2.0	Parameter of ball
Young's modulus of the parallel bond (GPa)	14.6	Parameter of ball
Ratio of normal to shear stiffness of the parallel bond	3.0	Parameter of ball
Parallel bond normal strength, mean (MPa)	27	Parameter of parallel bond
Parallel bond normal strength, standard deviation (MPa)	5.4	Parameter of parallel bond
Parallel bond shear strength, mean (MPa)	80	Parameter of parallel bond
Parallel bond shear strength, standard deviation (MPa)	16	Parameter of parallel bond

**Table 6** Micro-mechanical parameters for filling material in PFC<sup>2D</sup>

Micro-parameters	Values	Remarks
Friction coefficient	0.1	Parameter of ball
Minimum radius of the ball (mm)	0.3	Parameter of ball
Ratio of maximum to minimum radius	1.5	Parameter of ball
Normal stiffness of the ball (GN m <sup>-1</sup> )	6.8	Parameter of ball
Shear stiffness of the ball (GN m <sup>-1</sup> )	3.4	Parameter of ball
Normal stiffness of the parallel bond (MPa m <sup>-1</sup> )	88	Parameter of parallel bond
Shear stiffness of the parallel bond (MPa m <sup>-1</sup> )	29	Parameter of parallel bond
Parallel bond normal strength, mean (kPa)	246	Parameter of parallel bond
Parallel bond shear strength, mean (kPa)	571	Parameter of parallel bond

**Table 7** Comparison of experimental and numerical results for infilled specimens (MPa)

Specimen type	A	B	C	D	E	F	G
Experimental results	42.02	43.56	45.37	35.25	49.05	34.75	31.62
Numerical results	40.26	43.06	45.21	38.73	44.16	37.88	32.20
Deviation (%)	4.19	1.15	0.35	3.48	9.97	9.01	1.83

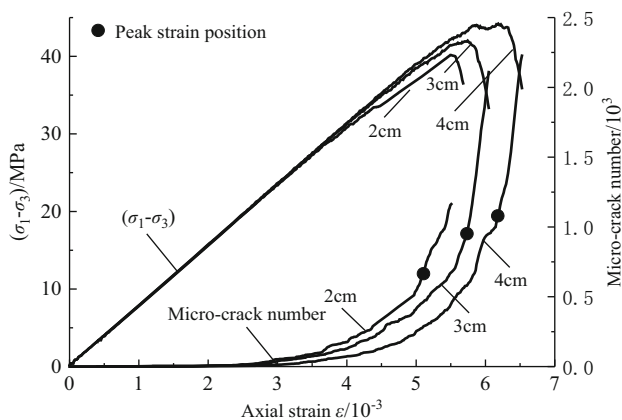


**Fig. 11** Stress–strain and micro-crack number–strain curves for specimens with different rock bridge

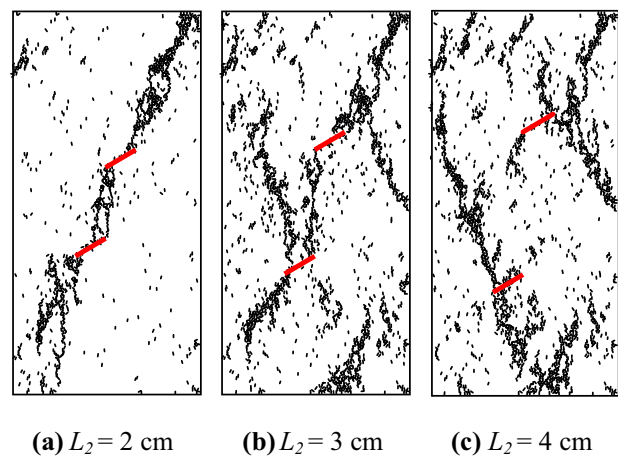


**Fig. 12** Distribution of micro-cracks in specimens with different rock bridge lengths

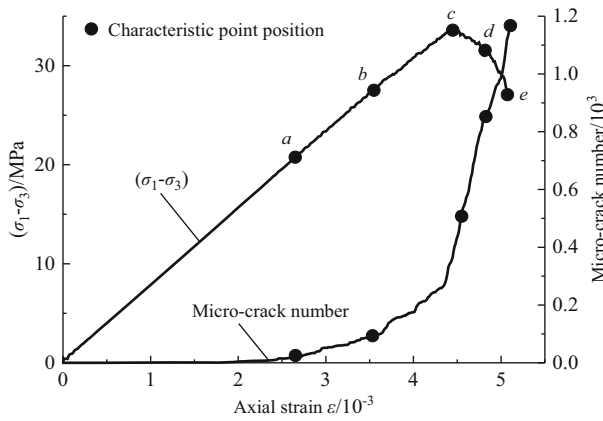


**Fig. 13** Stress–strain and micro-crack number–strain curves for specimens ( $L_2 = 2$  cm)

To analyse the crack coalescence process, five characteristic points in the loading process were selected to observe the micro-crack development process and porosity distribution for specimens with a rock bridge length of 2 cm. Figure 13 shows that the point *a* axial stress is

20.77 MPa (60%  $\sigma_1$ ), point *b* axial stress is 27.69 MPa (80%  $\sigma_1$ ), point *c* is the peak strength, point *d* axial stress is 31.15 MPa (90%  $\sigma_1$ ), and point *e* is the load terminating point.

From Figs. 13, 14 and 15, it can be seen that there are only fifteen micro-cracks in the sample at monitoring point *a*, which are distributed randomly and create small porosity in each part of the model. At monitoring point *b*, the number of micro-cracks in the specimen reaches 85, and inclined shear cracks appear at the tips of the flaws. The porosity of the model is similar to that of the model at point *a*. When the maximum principal stress reaches the peak strength (monitoring point *c*), the number of micro-cracks increases to 525. At this time, inclined shear cracks initiated at the tip of the flaws extend a slight distance outward first and then deflect and propagate towards the direction of the major principal stress. The tensile cracks at the internal flaw tip are connected, and the porosity increases slightly around the rock bridge. Then, the specimen enters the post-peak stage and reaches monitoring point *d*. At this time, the tensile crack initiated at the external tip of flaw 1 continues

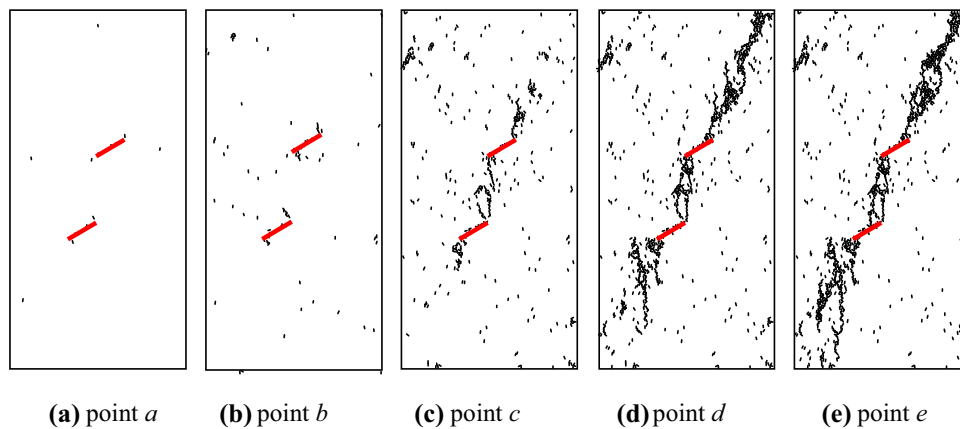


**Fig. 14** Micro-crack development of specimens during the loading process

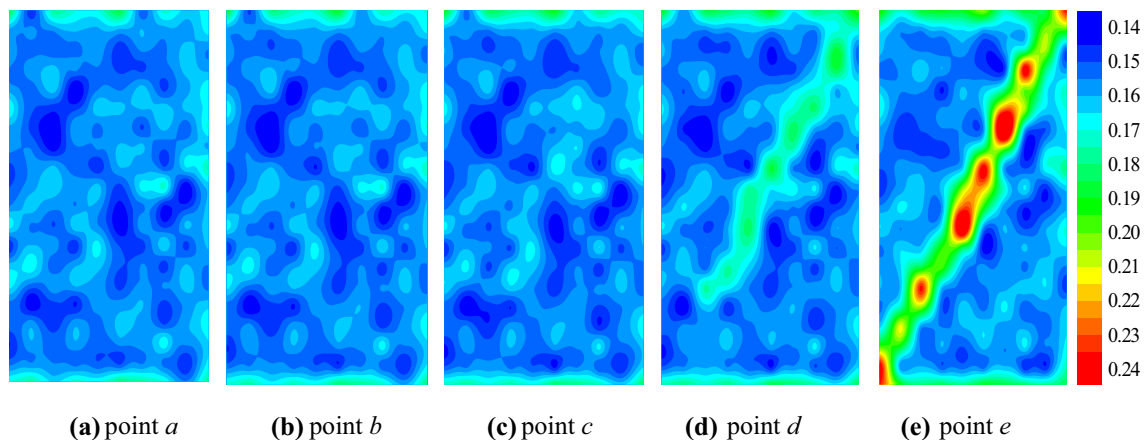


**Fig. 15** Porosity distribution of specimens during the loading process

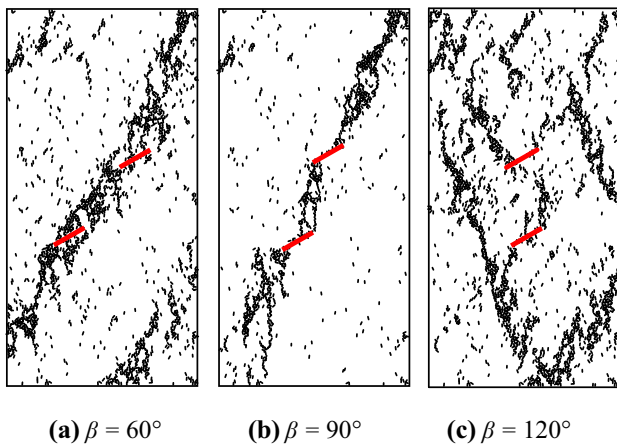


**Fig. 16** Distribution of micro-cracks in specimens with different rock bridge angles

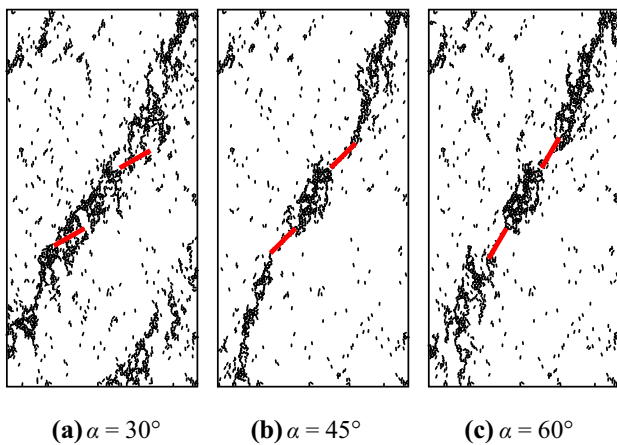


**Fig. 17** Distribution of micro-cracks in specimens with different flaw angles

to propagate and then penetrates to the top of the specimen. The tensile cracks developed in the rock bridge area form propagate farther and form elliptical cores, resulting in the failure of rock bridges. The external tip of flaw 2 continues to expand, and the intensity of micro-cracks increases significantly. In the process of moving from point *c* to point *d*, the number of micro-cracks increases from 525 to 956. From the porosity map, an obvious shear band appears at point *d* and penetrates the top of the specimen, which is consistent with micro-crack propagation. At the loading termination point *e*, the number of micro-cracks reaches a maximum of 1164, the density of tensile cracks at the external flaw tip is further increased, and the cracks at the external tip of flaw 2 bifurcate. The porosity of the model increases further, resulting in a shear fracture zone passing through the whole specimen. Due to the initiation, propagation, coalescence and penetration of cracks, tensile failure of the rock bridge and tensile–shear failure of the specimen occur.

Figures 16 and 17 show the distribution of cracks in the specimens with different rock bridge angles and different flaw angles under a confining pressure of 1 MPa, respectively. When the inclination angle of rock bridge is 60° and 90°, the rock bridges were damaged. When  $\beta = 60^\circ$ , there are dense crack zones around the flaws. These cracks form a wider fracture zone, but when  $\beta = 120^\circ$ , the rock bridges were not damaged. The specimen is the failure of the specimens with cracks along the ends of the two cracks. From Fig. 17, it can be seen that there are dense micro-cracks in the rock bridge area of the samples with different flaw angles, which indicates that the rock bridge is relatively fragmented. The fracture zones of the specimens with a flaw angle of 30° ( $\alpha = 30^\circ$ ) are relatively wide in the rock bridge area, while those with a flaw angle of 45° and a flaw angle of 60° are relatively narrow. The failure modes of all specimens are shear failure, which is caused by wing cracks or coplanar shear cracks at the tip of flaws. The failure mode, strength and crack trace of the specimens obtained by numerical experiments in this paper are basically in agreement with those obtained by laboratory tests. The validity of numerical experiments is verified.

## 5 Conclusions

In this paper, seven kinds of specimens with two infilled flaws were made in the laboratory. The crack evolution characteristics, failure modes and strength parameters of the specimens are studied by experimental tests and numerical tests. The main conclusions are as follows:

- There are two kinds of failure modes: shear failure and tensile–shear failure. The different flaw geometries are the main reasons for the different failure modes of the specimens. The cracks develop more easily along the interface between the model material and grouting material in the specimens with infilled flaws than in specimens with unfilled flaws.
- There are three main coalescence modes of rock bridges: tensile crack coalescence, shear crack coalescence and non-coalescence. When the rock bridge angle  $\beta = 60^\circ$ , the rock bridge undergoes mainly shear crack coalescence; when  $\beta = 90^\circ$ , the rock bridge experiences mainly tensile crack coalescence; when  $\beta = 120^\circ$ , the rock bridge does not coalesce.
- The peak strength of the specimen increases with increasing length and angle of the rock bridge and decreases with increasing fracture inclination angle. The shear strength parameters (cohesion and internal friction angle) of the specimens change nonlinearly with the influencing factors (rock bridge length, rock bridge angle and fracture angle).

- (d) The development of micro-cracks and the changes in porosity during the failure process of specimens with different rock bridge lengths are observed in the numerical tests. Tensile cracks are observed in the specimens when the axial stress reaches 80% of the peak strength, and an elliptical core appears in the specimens when the axial stress reached the peak strength. The number of cracks increases rapidly in the post-peak stage and finally causes a significant shear fracture zone. The strengths of the samples obtained from the numerical tests are consistent with those from the laboratory tests.

**Acknowledgements** This study is financially supported by the Natural Science Foundation of China (nos. 41672258, 41102162). The authors would also like to acknowledge the editors and reviewers of this paper for their very helpful comments and valuable remarks.

## References

- Moghadami M, Mortazavi A (2018) Development of a risk-based methodology for rock slope analysis. *Int J Civ Eng* 16(10):1317–1328
- Huang X, Liu QS, Liu B, Liu XW, Pan YC, Liu JP (2017) Experimental study on the dilatancy and fracturing behavior of soft rock under unloading conditions. *Int J Civ Eng* 15(6):921–948
- Tokiwa T, Tsusaka K, Aoyagi K (2018) Fracture characterization and rock mass damage induced by different excavation methods in the Horonobe URL of Japan. *Int J Civ Eng* 16(4):371–381
- Gratchev I, Kim DH, Yeung CK (2016) Strength of rock-like specimens with pre-existing cracks of different length and width. *Rock Mech Rock Eng* 49(11):4491–4496
- Haeri H, Shahriar K, Marji MF, Moarefvand P (2014) Cracks coalescence mechanism and cracks propagation paths in rock-like specimens containing pre-existing random cracks under compression. *J Cent South Univ* 21(6):2404–2414
- Abdollahipour A, Fatehi MM (2017) Analyses of inclined cracks neighboring two iso-path cracks in rock-like specimens under compression. *Geotech Geol Eng* 35(1):169–181
- Fan X, Li KH, Lai HP, Xie YL, Cao RH, Zheng J (2018) Internal stress distribution and cracking around flaws and openings of rock block under uniaxial compression: a particle mechanics approach. *Comput Geotech* 102:28–38
- Fan X, Li KH, Lai HP, Zhao QH, Sun ZH (2018) Experimental and numerical study of the failure behavior of intermittent rock joints subjected to direct shear load. *Adv Civ Eng* 2018:1–19
- Sun SR, Sun HY, Wang YJ, Wei JH, Liu J, Kanungo DP (2014) Effect of the combination characteristics of rock structural plane on the stability of a rock-mass slope. *Bull Eng Geol Environ* 73(4):987–995
- Cao RH, Cao P, Lin H, Pu CZ, Ou K (2016) Mechanical behavior of brittle rock-like specimens with pre-existing fissures under uniaxial loading: experimental studies and particle mechanics approach. *Rock Mech Rock Eng* 49(3):763–783
- Zhao YL, Zhang LY, Wang WJ, Pu CZ, Wan W, Tang JZ (2016) Cracking and stress–strain behavior of rock-like material containing two flaws under uniaxial compression. *Rock Mech Rock Eng* 49(7):2665–2687
- Cao P, Liu TY, Pu CZ, Lin H (2015) Crack propagation and coalescence of brittle rock-like specimens with pre-existing cracks in compression. *Eng Geol* 187:113–121
- Wang M, Cao P, Wan W, Zhao YL, Liu J, Liu JS (2017) Crack growth analysis for rock-like materials with ordered multiple pre-cracks under bi axial compression. *J Cent South Univ* 24(4):866–874
- Huang YH, Yang SQ, Tian WL, Zeng W, Yu LY (2016) An experimental study on fracture mechanical behavior of rock-like materials containing two unparallel fissures under uniaxial compression. *Acta Mech Sin* 32(3):442–455
- Feng P, Dai F, Liu Y, Xu NW, Du HB (2019) Coupled effects of static–dynamic strain rates on the mechanical and fracturing behaviors of rock-like specimens containing two unparallel fissures. *Eng Fract Mech* 207:237–253
- Wang M, Cao P (2017) Experimental study of crack growth in rock-like materials containing multiple parallel pre-existing flaws under biaxial compression. *Geotech Geol Eng* 35(3):1023–1034
- Xiao TL, Huang M, Cheng C, He YL (2018) Experimental investigation on the mechanical characteristics and deformation behavior of fractured rock-like material with one single fissure under the conventional triaxial compression. *Shock Vib* 2018:1–11
- Mirzaghobanali A, Nemcik J, Aziz N (2014) Effects of cyclic loading on the shear behavior of infilled rock joints under constant normal stiffness conditions. *Rock Mech Rock Eng* 47(4):1373–1391
- Liu RC, Jing HW, He LX, Zhu TT, Yu LY, Su HJ (2017) An experimental study of the effect of fillings on hydraulic properties of single fractures. *Environ Earth Sci* 76(20):684
- Shrivastava AK, Rao KS (2018) Physical modeling of shear behavior of infilled rock joints under CNL and CNS boundary conditions. *Rock Mech Rock Eng* 51(1):101–118
- Jahani H, Sadaghiani MH (2015) Experimental study on the shear strength of sandy clay infilled regular rough rock joints. *Rock Mech Rock Eng* 48(3):907–922
- Ma H, Liu QS (2017) Prediction of the peak shear strength of sandstone and mudstone joints infilled with high water-cement ratio grouts. *Rock Mech Rock Eng* 50(8):2021–2037
- Sagong M, Bobet A (2002) Coalescence of multiple flaws in a rock-model material in uniaxial compression. *Int J Rock Mech Min* 39(2):229–241
- Yu J, Chen X, Cai YY, Li H (2016) Triaxial test research on mechanical properties and permeability of sandstone with a single joint filled with gypsum. *KSCE J Civ Eng* 20(6):2243–2252
- Papaliangas T, Hencher SR, Lumsden AC, Manolopoulou S (1993) The effect of frictional fill thickness on the shear strength of rock discontinuities. *Int J Rock Mech Min Sci Geomech Abstr* 30(2):81–91
- Saeb S, Amadei B (1992) Modelling rock joints under shear and normal loading. *Int J Rock Mech Min Sci Geomech Abstr* 29(3):267–278
- Indraratna B, Welideniya HS, Brown ET (2005) A shear strength model for idealised infilled joints under constant normal stiffness. *Geotechnique* 55(3):215–226
- Liu J, Wang J (2018) Stress evolution of rock-like specimens containing a single fracture under uniaxial loading: a numerical study based on particle flow code. *Geotech Geol Eng* 36(1):567–580
- Li G, Liang ZZ, Tang CA (2015) Morphologic interpretation of rock failure mechanisms under uniaxial compression based on 3D multiscale high-resolution numerical modeling. *Rock Mech Rock Eng* 48(6):2235–2262
- Tang CA, Lin P, Wong RHC, Chau KT (2001) Analysis of crack coalescence in rock-like materials containing three flaws—Part II: numerical approach. *Int J Rock Mech Min* 38(7):925–939

31. Wong RHC, Tang CA, Chau KT, Lin P (2002) Splitting failure in brittle rocks containing pre-existing flaws under uniaxial compression. *Eng Fract Mech* 69(17):1853–1871
32. Liu HY, Zhang YD (2018) Numerical simulation of the failure process and mechanical behavior of a rock material with non-persistent cracks under compression. *Arab J Sci Eng* 43(7):3673–3683
33. Cheng H, Zhou XP, Zhu J, Qian QH (2016) The Effects of crack openings on crack initiation, propagation and coalescence behavior in rock-like materials under uniaxial compression. *Rock Mech Rock Eng* 49(9):3481–3494
34. Chong Z, Li X, Yao Q, Zhang J, Chen T (2016) Anchorage behavior of reinforced specimens containing a single fissure under uniaxial loading: a particle mechanics approach. *Arab J Geosci* 9(12):592
35. Yin Q, Jing H, Su H (2018) Investigation on mechanical behavior and crack coalescence of sandstone specimens containing fissure-hole combined flaws under uniaxial compression. *Geosci J* 22(5):825–842
36. Le HL, Sun SR, Kulatilake P, Wei JH (2018) Effect of grout on mechanical properties and cracking behavior of rock-like specimens containing a single flaw under uniaxial compression. *Int J Geomech* 18(10):04018129
37. Wong RHC, Chau KT (1998) Crack coalescence in a rock-like material containing two cracks. *Int J Rock Mech Min* 35(2):147–164
38. ASTM (2004) Standard test method for triaxial compressive strength of undrained rock core specimens without pore pressure measurements (Withdrawn 2005), ASTM D2664-04. ASTM, West Conshohocken, PA
39. Lajtai EZ (1974) Brittle fracture in compression. *Int J Fract* 10(4):525–536
40. Bobet A (2000) The initiation of secondary cracks in compression. *Eng Fract Mech* 66(2):187–219
41. Yang SQ, Jing HW (2011) Strength failure and crack coalescence behavior of brittle sandstone samples containing a single fissure under uniaxial compression. *Int J Fract* 168(2):227–250
42. Park CH, Bobet A (2009) Crack coalescence in specimens with open and closed flaws: a comparison. *Int J Rock Mech Min* 46(5):819–829
43. Wong LNY, Einstein HH (2009) Systematic evaluation of cracking behavior in specimens containing single flaws under uniaxial compression. *Int J Rock Mech Min* 46(2):239–249
44. Sun HY (2015) Research on fracture mechanism of non-penetrative jointed rock mass based on random structure plane. Master thesis, Hohai University, Nanjing (**in Chinese**)
45. Le HL, Sun SR, Wei JH (2019) Influence of types of grouting materials on compressive strength and crack behavior of rocklike specimens with single grout-infilled flaw under axial loads. *J Mater Civ Eng* 31(1):06018022
46. Zhuang XY, Chun JW, Zhu HH (2014) A comparative study on unfilled and filled crack propagation for rock-like brittle material. *Theor Appl Fract Mech* 72(1):110–120
47. Cho N, Martin CD, Segol DC (2007) A clumped particle model for rock. *Int J Rock Mech Min* 44(7):997–1010
48. Potyondy DO, Cundall PA (2004) A bonded-particle model for rock. *Int J Rock Mech Min* 41(8):1329–1364